PHILOSOPHICAL TRANSACTIONS A

royalsocietypublishing.org/journal/rsta

Probabilistic buckling of imperfect hemispherical shells containing a distribution of defects

Fani Derveni†, William Gueissaz†, Dong Yan and Pedro M. Reis

Ecole Polytechnique Fédérale de Lausanne (EPFL), Flexible Structures Laboratory, 1015 Lausanne, Switzerland

FD, 0000-0001-8159-0345; WG, 0000-0003-3251-8448; DY , 0000-0002-7988-3031; PMR, 0000-0003-3984-828X

Research

Cite this article: Derveni F, Gueissaz W, Yan D, Reis PM. 2023 Probabilistic buckling of imperfect hemispherical shells containing a distribution of defects. *Phil. Trans. R. Soc. A* **381**: 20220298.
https://doi.org/10.1098/rsta.2022.0298

Received: 31 August 2022
Accepted: 12 October 2022

One contribution of 13 to a theme issue 'Probing and dynamics of shock sensitive shells'.

Subject Areas:
structural engineering, mechanical engineering, mechanics

Keywords:
probabilistic buckling, random imperfections, knockdown factors, experiments, finite-element modelling, micro-computed tomography

Author for correspondence:
Pedro M. Reis
e-mail: pedro.reis@epfl.ch

The buckling of spherical shells is plagued by a strong sensitivity to imperfections. Traditionally, imperfect shells tend to be characterized empirically by the knockdown factor, the ratio between the measured buckling strength and the corresponding classic prediction for a perfect shell. Recently, it has been demonstrated that the knockdown factor of a shell containing a single imperfection can be predicted when there is detailed *a priori* knowledge of the defect geometry. Still, addressing the analogous problem for a shell containing many defects remains an open question. Here, we use finite element simulations, which we validate against precision experiments, to investigate hemispherical shells containing a well-defined distribution of imperfections. Our goal is to characterize the resulting knockdown factor statistics. First, we study the buckling of shells containing only two defects, uncovering non-trivial regimes of interactions that echo existing findings for cylindrical shells. Then, we construct statistical ensembles of imperfect shells, whose defect amplitudes are sampled from a lognormal distribution. We find that a 3-parameter Weibull distribution is an excellent description for the measured statistics of knockdown factors, suggesting that shell buckling can be regarded as an extreme-value statistics phenomenon.

This article is part of the theme issue 'Probing and dynamics of shock sensitive shells'.

†These authors contributed equally to this study.

Electronic supplementary material is available online at https://doi.org/10.6084/m9.figshare.c.6373233.

THE ROYAL SOCIETY PUBLISHING

1. Introduction

Thin shell structures with their inherent curved, slender configurations, have been studied extensively across a wide range of length scales, from viruses [1], pollen grains [2] and plants [3], to drug-delivery capsules [4], gas tanks [5] and aeronautical structures [6]. Owing to their slenderness, shells are prone to buckling, whose subcritical nature can cause the catastrophic loss of load-bearing capacity and sudden changes in the deformation mode [7]. Whereas shell buckling is often regarded as a phenomenon to avoid in traditional structural mechanics, recent studies have enlightened the benefits of leveraging the buckled configurations in attaining advantageous mechanical properties [8–10]. These studies reflect the change in perspective from *buckliphobia* to *buckliphilia* [11].

For the design of shell structures, it is desirable to have accurate predictions for their limits of stability. The pioneering work of Zoelly [12] provides the widely used prediction for the critical buckling condition of a pressurized perfect spherical shell:

$$p_\mathrm{c} = \frac{2E}{\sqrt{3(1-\nu^2)}}\eta^{-2}, \tag{1.1}$$

where E is Young's modulus, ν is Poisson's ratio and $\eta = R/t$ is the radius (R) to thickness (t) ratio, measuring the slenderness of the spherical shell. Subsequently, a large body of experimental studies has shown that equation (1.1) systematically overpredicts experimental measurements [13–18], due to a strong sensitivity of the buckling to material and/or geometric imperfections. Koiter [19] proposed a general theory of elastic stability to study the post-buckling behaviour of structures. Instigated by this seminal work, much theoretical effort has been dedicated to study shell buckling in the presence of assumed imperfections in geometry, loading and boundary conditions [20–24]. Still, given the lack of theoretical bases to predict their critical buckling strength, realistic (imperfect) shells tend to be characterized empirically by the *knockdown factor*,

$$\kappa = \frac{p_\mathrm{max}}{p_\mathrm{c}}, \tag{1.2}$$

where p_max is the measured maximum buckling pressure supported by the shell and p_c is the corresponding classic prediction from equation (1.1) if the shell were to be perfect. For example, NASA has largely relied on knockdown factors in the characterization of shell structures [25,26], using vast experimental datasets to devise empirical guidelines to aid the design of imperfection-sensitive shells.

Significant progress in the experimental study of shell buckling was made recently, in part due to the introduction of a versatile shell fabrication technique proposed by Lee *et al.* [27]. By coating a rigid hemispherical mould with a liquid polymer solution, this technique yields a shell of nearly uniform thickness upon curing. Lee *et al.* [28] then used a flexible mould, deformed by an indenter applied at the pole, to produce shells containing a single, precisely engineered, dimple-like defect. Importantly, this technique by Lee *et al.* [28] offers precise and systematic control over the geometry of the engineered defect, enabling accurate and thorough measurements of the knockdown factor as a function of the imperfections characteristics. Their experimental results evidenced that, as the amplitude of a single dimple-like defect increases, the knockdown factor decreases rapidly until it reaches a plateau, the onset of which occurs when the defect amplitude is approximately equal to the shell thickness. The authors also demonstrated that when the geometry of the imperfection is known in detail, the knockdown factor can be predicted accurately, either through finite-element modelling or reduced-order shell theory models. The dependence of the knockdown factor and its plateau on the geometric parameters of the defect and the shell has also been studied in detail [29]. All of these results for imperfect spherical shells are qualitatively consistent with much earlier theoretical analyses for cylindrical shells [21], but this time with accurate quantitative predictions validated by precision experiments. The case of a through-thickness single imperfection on a hemispherical shell has also been studied [30].

All the aforementioned studies measured the knockdown factor by buckling the imperfect shells. As an alternative, a non-destructive poking technique was proposed in [31,32] to probe the critical buckling load of an imperfect cylindrical shell from its response to indentation at different axial loading levels to extrapolate the critical conditions without actually breaking the shell. This technique has also been successfully applied to spherical shells [33,34]. Further experimental and numerical studies revealed that, due to the localized deformation caused by the defect, the reliability of the poking test is strongly affected by the distance between the poking location and the imperfections, for both cylindrical [35,36] and spherical shells [33,34]. Particularly, Fan *et al.* [35] performed numerical poking tests on shells with two dimple-like defects and with a distribution of defects measured from an aluminium can. They showed that the poker had to be positioned sufficiently close to the centre of the most deleterious defect in order to yield accurate predictions.

Despite the significant advances mentioned above in theoretical, experimental and computational studies of shells containing a single imperfection, there remain many open questions in the more realistic and practically relevant case of shell buckling due to multiple, or even a large distribution of imperfections, potentially influenced by defect–defect interactions. Wullschleger [37] studied imperfect cylindrical shells containing two defects at varying levels of separation, and showed that the interactions become important when the defects are close to each other. Beyond the two-defect case, various probabilistic methods to predict the knockdown factor of cylindrical shells have been proposed. Axisymmetric defects on cylindrical shells were investigated in the earlier work of Amazigo [38] via a modified truncated hierarchy method, concluding that the buckling capacity depends on the spectral imperfection density. Cylindrical shells with random imperfections subjected to axial compression have also been examined using the Monte Carlo method, imposing either axisymmetric [39] or asymmetric [40] defects. These studies established probabilistic methods as the more suitable approach to assess the design criteria for cylindrical shells when compared with deterministic approaches. These various probabilistic methods relevant for shell buckling have been reviewed by Elishakoff [41]. However, for spherical shells, to the best of our knowledge, the influence of defect–defect interactions on their buckling behaviour has not been reported to date. Furthermore, statistics of the knockdown factor for spherical shells containing distributions of defects remain mostly unexplored.

Here, we investigate the buckling of imperfect hemispherical shells containing a large number of defects, and compare the statistics of knockdown factors with the classical case of single-defect shell buckling. Our study follows two stages, combining experiments and simulations. First, we fabricate elastomeric hemispherical shells using three-dimensionally printed moulds containing several imperfections and a polymer-coating technique. We characterize the full three-dimensional geometry of the experimental specimens using X-ray micro-computed tomography (μCT). Finally, we obtain knockdown factors via physical buckling tests, which are then used to validate the finite-element method (FEM) simulations. Second, we turn our attention to the validated FEM and study the two-defect case where the distance between the two defects is systematically varied, uncovering a possible interaction regime. Then we construct statistical ensembles of shells, each containing a large number of defects whose amplitude is treated as a lognormal distributed random variable. By simulating the buckling of these ensembles of imperfect shells using FEM, we compute the knockdown factor statistics. Our results show that the probability density function (PDF) of the knockdown factor is described well by a Weibull distribution. We also find that the mode (peak) of the knockdown factor PDF decreases when both the mean defect amplitude and its standard deviation increase. In addition, when the minimum distance between defects is large, we observe that the knockdown factors are exclusively dominated by the largest defect, similar to what is observed in the single-defect case. However, when the minimum separation decreases, defect–defect interactions play a significant role in dictating the knockdown factor. Our findings suggest that shell buckling can be placed in the broader class of extreme-value statistics phenomena, calling for the study of probabilistic shell buckling in even more practically relevant imperfection conditions.

royalsocietypublishing.org/journal/rsta *Phil. Trans. R. Soc. A* **381**: 20220298

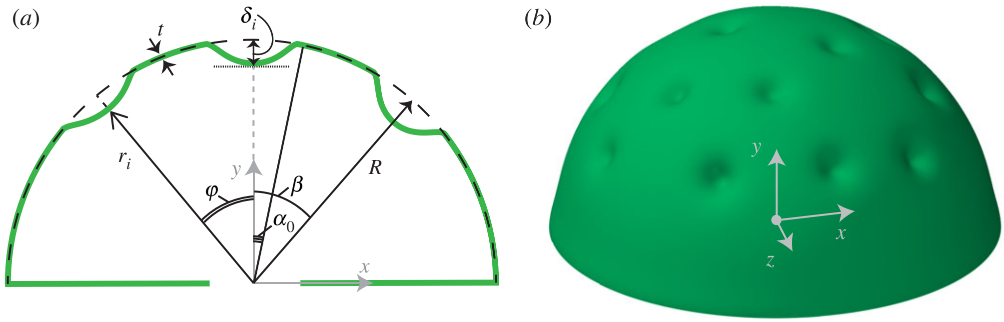

Figure 1. Problem definition. (*a*) A two-dimensional schematic of an elastic hemispherical shell with three dimple defects. (*b*) A three-dimensional representation of a shell with multiple dimple imperfections, w_i (equation (2.1)), whose amplitudes, $\overline{\delta}_i$, follow a lognormal distribution (equation (2.5)). (Online version in colour.)

Our paper is structured as follows. In §2, we define the problem and state the main research questions. Section 3 presents the experimental methodology, including (a) the protocol to fabricate the imperfect shells, (b) the characterization of their geometry using X-ray μCT and (c) the experimental pressure-buckling tests. Section 4 details the FEM simulations, which are then validated against experiments in §5. Section 6 is dedicated to the case of an imperfect shell containing two defects. Results of the buckling statistics for shells containing a distribution of imperfections are presented in §7. Section 8 provides the conclusions of our work, including a discussion of our findings and recommendations for future work.

2. Definition of the problem

We consider a thin, elastic and hemispherical shell containing a distribution of geometric imperfections, as illustrated in figure 1. The overall geometry of the shell is described by its nominal radius, R, and thickness, t, with a radius-to-thickness ratio $\eta = R/t$. The shell contains $N > 1$ (typically $N \gg 1$) defects, each of which is assigned an index i. The ith defect introduces a radial deviation, w_i, of the otherwise spherical mid-surface of the shell. Following the work of Lee *et al.* [28], we assume that each of these imperfections is shaped as a Gaussian dimple,

$$w_i(\alpha) = -\delta_i \, \mathrm{e}^{-(\alpha/\alpha_0)^2}, \tag{2.1}$$

where the variable α is the *local* angular distance (spherical coordinate) from the centre of the defect, and the constants δ_i and α_0 are, respectively, the amplitude (maximum radial deviation of the mid-surface) and half-angular width of the ith defect. The defect amplitude is non-dimensionalized by the shell thickness, $\overline{\delta}_i = \delta_i/t$. Hereon, when referring to the defect amplitudes (and associated quantities such as the mean and standard deviation of its distribution), we shall mean their dimensionless versions. Also, following a standard in the literature [42,43], we use the following geometric parameter to characterize the defect width:

$$\lambda = [12(1-\nu^2)]^{1/4} \, \eta^{1/2} \, \alpha_0. \tag{2.2}$$

As shown schematically in figure 1*a*, the location on the shell's mid-surface of the centre of each defect (where the local angle is $\alpha = 0$) is defined by the unit radial vector:

$$\mathbf{e}_{r_i} = \sin\beta_i \cos\theta_i \mathbf{e}_x + \cos\beta_i \mathbf{e}_y + \sin\beta_i \sin\theta_i \mathbf{e}_z, \tag{2.3}$$

where β_i and θ_i are specific values of the *global* zenith (polar) and azimuthal spherical coordinates, β and θ, respectively, associated with the ith defect. Note that the *local* angle, α in equation (2.1), associated with each defect, can be related to (β, θ) and their specific values for the defect centre

(β_i, θ_i) but this complicated function is unnecessary to define the geometry. The pole of the shell is located at $\beta = 0$ and the origin of the Cartesian coordinate system ($\mathbf{e}_x$, $\mathbf{e}_y$, $\mathbf{e}_z$) is located at the centre of the circular base of the hemisphere. The radial distance of the middle surface of the shell is $r_\mathrm{m}(\beta, \theta) = R + \sum_{i=1}^{N} w_i(\beta, \theta)$. The centre of each defect is at a distance $b_i = r_\mathrm{m}(\beta_i, \theta_i) = R - \delta_i$ from the origin and its radial position vector is $\mathbf{r}_i = b_i \mathbf{e}_{r_i}$. The angular separation between two neighbouring defects, i and j, whose centres are located at $\mathbf{e}_{r_i}$ and $\mathbf{e}_{r_j}$, is defined as

$$\varphi_{(i,j)} = \left| \arccos(\mathbf{e}_{r_i} \cdot \mathbf{e}_{r_j}) \right|. \tag{2.4}$$

If the ith defect is located at the pole ($\beta = 0$), then $\varphi_{(i,j)} = \beta_j$, but this is not so in the general case of $\beta_i \neq \beta_j \neq 0$ and $\theta_i \neq \theta_j$.

First, we will address the buckling problem of a shell containing only two imperfections ($N = 2$), seeking to characterize the effect of defect–defect interactions. To this end, with $i = \{1, 2\}$, we systematically vary the defect amplitudes, $\overline{\delta}_i$, geometric parameter, λ_i, and their angular (centre-to-centre) separation, $\varphi_{(1,2)}$. The $i = 1$ defect is positioned at the shell pole ($\beta = 0$) and the $i = 2$ defect at a polar location β_2, such that $\varphi_{(1,2)} = \beta_2$. We aim to quantify how the knockdown factor of this imperfect shell depends on $\overline{\delta}_i$, λ_i and $\varphi_{(1,2)}$. For the explored $N = 2$ configurations, we will consider two cases for the defects' geometric parameters and amplitudes: one with $\lambda = \lambda_1 = \lambda_2$ and $\overline{\delta} = \overline{\delta}_1 = \overline{\delta}_2$, and another with $\lambda_1 \neq \lambda_2$ and $\overline{\delta}_1 \neq \overline{\delta}_2$. In both cases, we will find that the knockdown factor, κ, exhibits a non-trivial behaviour as a function of $\varphi_{(1,2)}$; these results are reported in §6. The defect–defect interactions will be important when setting up and interpreting the more complex problem of buckling of imperfect shells with a large distribution ($N \gg 1$) of defects, introduced next.

In our second and central problem, we build upon past studies on the sensitivity of the buckling of spherical defects containing a *single* defect [24,28,29,33] to now consider imperfect shells with a *large number* ($N \gg 1$) of randomly distributed defects. Specifically, we design shells whose defects have a statistical distribution of amplitudes $\overline{\delta}_i$ (lognormally distributed) and positions $\mathbf{r}_i$ (distributed according to a random sequential adsorption algorithm). These designs explore a few fixed values of the defect angular width, α_0, and hence λ through equation (2.2). The PDF of the defect amplitude is:

$$f(\overline{\delta}_i) = \frac{1}{\overline{\delta}_i \sigma \sqrt{2\pi}} \exp\left(-\frac{(\ln \overline{\delta}_i - \mu)^2}{2\sigma^2} \right), \tag{2.5}$$

where μ and σ are parameters related to the mean defect amplitude

$$\langle \overline{\delta} \rangle = \exp\left(\mu + \frac{\sigma^2}{2} \right), \tag{2.6}$$

and its standard deviation

$$\Delta\overline{\delta} = \left\{ [\exp(\sigma^2) - 1] \exp(2\mu + \sigma^2) \right\}^{1/2}. \tag{2.7}$$

Note that the logarithms of the defect amplitudes, $\ln(\overline{\delta})$, are normally distributed with mean μ and standard deviation σ. One advantage of using a lognormal PDF in seeding the imperfections is that it establishes positive values of $\overline{\delta}_i$, ensuring that we only deal with dimples (and not a combination of dimples and bumps). Also, lognormal distributions of imperfections are used widely in structural reliability analysis [44–47].

The position of each defect, defined in equation (2.3), is seeded randomly onto the shell, one by one, using a random sequential adsorption algorithm [48–50], which is commonly used to generate nearly isotropic porous structures. Here, we modify the volumetric case to randomly distribute circles on the hemispherical surface of a shell. Overlaps are avoided by setting a minimum angular separation between defects, φ_min. The seeding procedure stops when the spherical cap delimited by a maximum zenith angle, β_max, no longer admits a new defect. We chose $\beta_\mathrm{max} = 60°$ to minimize interaction effects with the boundaries. For example, this seeding procedure with $\lambda = 1$ and $\beta_{\max} = 60^\circ$ yields $N \approx 80$ defects. The seeding algorithm will be described in more detail in §3a.

The hemispherical, imperfect shell with N random defects, is clamped at its equator and loaded under negative pressure, p_0. When the imposed pressure difference reaches the critical value, $p_{\max}$, the shell buckles through a subcritical bifurcation. The case of a single imperfection, $N = 1$, has been addressed in previous studies [24,28,29,33,34], as described in the Introduction. In the present work, we seek to characterize the knockdown factor of shells with $N \geq 2$. First, we focus on the defect–defect interactions in the $N = 2$ case, and then we turn to the probabilistic case with $N \gg 1$ defects. We systematically vary the mean, $\langle\bar{\delta}\rangle$, and standard deviation, $\Delta\bar{\delta}$, of the seeding lognormal distribution, while fixing λ and $\varphi_{\min}$. Statistical ensembles of imperfect shells with statistically equivalent configurations are produced for each set of parameters, $(\langle\bar{\delta}\rangle, \Delta\bar{\delta}, \lambda, \varphi_{\min})$.

Producing a large number of realizations is impractical in experiments. As such, in the second stage of our investigation, we will perform a systematic statistical investigation using the FEM simulations exclusively. Trust on the FEM will be built up by a prior direct quantitative validation against a few specific experimental cases. For practical reasons, the experiments (and, hence, the FEM validation) will be performed for shells with *outward* (bump) defects, instead of the *inward* (dimple) defects in equation (2.1). This choice is motivated by limitations during the fabrication of the experimental specimens, as detailed in §3a.

The experimentally validated FEM will then be leveraged to simulate the buckling of statistical ensembles of imperfect shells, designed with either $N = 2$ or $N \gg 1$ defects, as described above. The probabilistic results will be interpreted in light of previous findings [28] for $N = 1$, together with the case of $N = 2$ (§6). The latter includes the possibility of defect–defect interactions, which are important for the $N \gg 1$ probabilistic case. Ultimately, the primary question we tackle is: *Given an input set of statistics for the design geometry of the imperfect shells, what are the output statistics of the resulting knockdown factors, κ, as characterized by the probability density function, $f(\kappa)$?*

3. Methods: experiments

We proceed by describing the experimental fabrication and characterization of shell specimens containing multiple defects, as well as the experimental protocol followed to measure their critical buckling conditions under pressure loading.

Previous experimental studies on shell buckling [28,30,33,34,51] have employed a coating technique [27] to fabricate elastomeric shells of nearly constant thickness, containing a single well-defined geometric imperfections. Toward tackling the problem defined in §2, while building on past work, we have developed a novel experimental technique using three-dimensionally printed moulds, enabling the robust fabrication of shells containing *multiple* defects, whose geometry, number and layout can be designed precisely.

The exact geometry of the experimental shells is different from the idealized geometry described in §2 (cf. figure 1); however, the high precision buckling tests described in §3c will serve as a thorough quantitative validation of FEM (§5). For validation of the simulations, the full geometry of the fabricated shells is quantified using X-ray μCT and is imported into the FEM (§4). After validating the FEM, the buckling of imperfect shells with $N \geq 2$ is more systematically explored using the simplified geometry of §2; these results will be presented in §§6 and 7.

(a) Design and fabrication of imperfect shell specimens

We produced textured hemispherical moulds using a desktop stereolithography three-dimensional printer (Form 2 Formlabs) using Clear V4 resin (figure 2*a*), with a resolution of 25 µm per layer. Throughout, the nominal radius of the moulds is fixed at $R = 25.4$ mm.

The imperfections are introduced by design into the surface of the spherical mould, with several small spherical protrusions of radius $s \ll R$ to produce defects as *bumps* (figure 2*c*). The centre of each of these spherical bumps is located at a distance d_i from the centre of the nominal

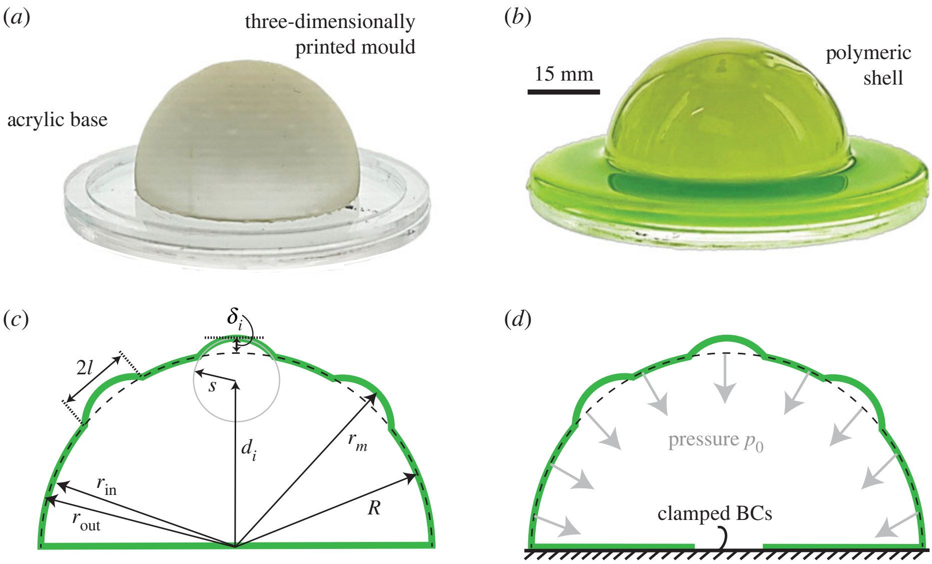

Figure 2. Fabrication and design of the imperfect shell specimens. (*a*) Representative photograph of the three-dimensionally printed mould containing several defects (bumps). Owing to the small size of the bumps, they are not visible at naked eye in the photograph. (*b*) The mould is coated with a liquid film of VPS-32, which upon curing and demoulding yields the thin hemispherical shell. (*c*) Schematic diagram of the shell geometry. (*d*) The hemispherical shell is clamped at the equator and depressurized to measure the critical buckling conditions. (Online version in colour.)

sphere of radius R, so that they produce a maximum radial distance $\delta_i = d_i + s - R$. The defect width is defined by the intersection between the bump and the nominal sphere of the mould, and computed from geometry [52] as

$$l = \frac{1}{2d_i}\sqrt{4d_i^2R^2 - (d_i^2 - s^2 + R^2)^2}. \tag{3.1}$$

A number of bumps protruding from a hemisphere is seeded onto the mould surface, with well-defined statistics for $\overline{\delta}_i$ and l, and using the same random sequential adsorption algorithm mentioned in §2. The seeding is performed within a spherical cap of the mould, delimited by a threshold value of the zenith angle $\beta_{\max}$, to avoid potential interactions with the equatorial boundary when the shell is fabricated (more on this below). Within this cap, we randomly sample the angular position of the centre of each ith defect,

$$\left(\beta_i, \theta_i\right) = \left(\arccos(1 - x_\beta(1 - \cos\beta_{\max})),\ 2\pi x_\theta\right), \tag{3.2}$$

where $x_\beta \in [0, 1]$ and $x_\theta \in [0, 1]$ are two random variables with an equal probability to locate the defect anywhere on the hemisphere cap. The algorithm also imposes a constraint on the angle between the centres of any pair of defects (with indices i and j),

$$\varphi_{(i,j)} \geq \varphi_{\min}, \tag{3.3}$$

such that $\varphi_{\min} \geq 2\alpha_0 = 2\arcsin(l/R)$. For each shell design with fixed l, every new ith defect is seeded at a random location of the shell and tested for equation (3.3), with respect to all other already existing defects ($j = 1, \ldots, i-1$). If equation (3.3) is satisfied, a new $i+1$ defect is seeded with the same procedure. If equation (3.3) is not satisfied, this ith defect is removed, and a new random location is generated until a valid condition is attained, up to a given maximum number (10^6) of attempts. When this number of attempts is reached, the seeding process stops, setting the final number of defects, N.

royalsocietypublishing.org/journal/rsta *Phil. Trans. R. Soc. A* **381**: 20220298

Table 1. Design parameters of the shells with bumps fabricated in the experiments (see §3a) and simulated via FEM for validation (see §5): average $\langle\bar{\delta}\rangle$ and standard deviation $\Delta\bar{\delta}$ of defect amplitude, geometric (width) parameter λ, minimum angle between defect centres $\varphi_{\min}$, maximum zenith angle $\beta_{\max}$ and number of defects N.

specimen no.	λ (—)	$\langle\bar{\delta}\rangle$ (—)	$\Delta\bar{\delta}$ (—)	$\varphi_{\min}$ (°)	$\beta_{\max}$ (°)	N (—)
Shell 1	0.539	0.643	0.000	6.189	20	7
Shell 2	1.056	0.575	0.000	9.446	20	7
Shell 3	0.553	0.794	0.180	4.790	20	24
Shell 4	2.205	0.769	0.000	20.000	20	1
Shell 5	1.571	0.698	0.000	14.787	60	30
Shell 6	2.188	0.757	0.166	18.717	60	17
Shell 7	1.889	0.865	0.000	18.488	60	20
Shell 8	3.519	2.143	0.000	34.954	60	5

The amplitude of each of the defects is treated as a random variable using a normal distribution, $\bar{\delta}_i \sim \mathrm{Normal}(\langle\bar{\delta}\rangle, \Delta\bar{\delta}^2)$, with mean $\langle\bar{\delta}\rangle$ and standard deviation $\Delta\bar{\delta}$. Note that the normal distribution used for the experimental specimens (with *outward* bumps) is only employed in the experiments geared to validate the FEM simulations in §5. The FEM simulations in §§6 and 7 use designs generated with a lognormal distribution (with *inward* dimple) (cf. equations (2.1) and (2.5)). The reason for this disparity is practical: we first performed the experiments before realizing that lognormal-distributed defects were a better choice, but it was then impractical to redo all experiments with the new design. Regardless of the design details, the experiments are appropriate for the detailed validation of the FEM before turning to the more thorough and systematic numerical exploration of the problem defined in §2.

We have designed and three-dimensionally printed eight different moulds, whose geometric parameters are detailed in table 1. Four of the moulds had bumps in the spherical cap within $\beta_{\max} = 20°$ and the other four within $\beta_{\max} = 60°$. The explored ranges of the design parameters were: $0.5 < \lambda < 4.0$, $0.5 < \langle\bar{\delta}\rangle < 2.5$ and $5° < \varphi_{\min} < 35°$. Consequently, these parameters set the range of the number of defects: $1 \le N \le 30$. Note that Shell 4 corresponds to a mould containing a single defect, which is achieved by setting $\varphi_{\min} = \beta_{\max}$.

Each hemispherical shell is fabricated by pouring vinylpolysiloxane (VPS-32, Elite Double 32, Zhermack) polymer onto the respective three-dimensionally printed mould, as shown in figure 2*b*. To emulate clamped boundary conditions of the fabricated shells during testing, a distance of 3 mm is set between the lower part of the printed mould and the centre of the hemisphere, allowing for the formation of a thick polymeric equatorial lip during the shell fabrication (figure 2*b*). The mould was mounted concentrically on the circular recess of a flat plate (depth 3 mm), whose top surface was aligned with the equator of the mould. Upon pouring, this recess was filled with the VPS-32 polymer solution, while avoiding overflow, to form an equatorial lip. The thickness of this lip (3 mm) was significantly thicker than the typical values of the shell thickness ($t \approx 0.3$ mm for Shells 1–7 and $t \approx 0.4$ mm for Shell 8). As such, this lip served to emulate clamped boundary conditions during the buckling tests (more on these below).

The VPS-32 polymer solution was prepared by mixing a base and a curing agent (1–1 weight ratio) in a centrifugal mixer (ARE-250, Thinky USA Inc., Laguna Hills, CA, USA) for 200 r.p.m./s clockwise and 220 r.p.m./s counterclockwise, a process that also removes air bubbles. After mixing, the VPS-32 solution was only poured onto the moulds after a quiescent waiting time of 3 min to control the viscosity of the solution when pouring, setting an appropriate value of the thickness of the gravity-driven lubrication flow down the surface of the mould [27]. After a curing time of 20 min, the liquid VPS-32 film solidified, and the resulting elastic shell containing

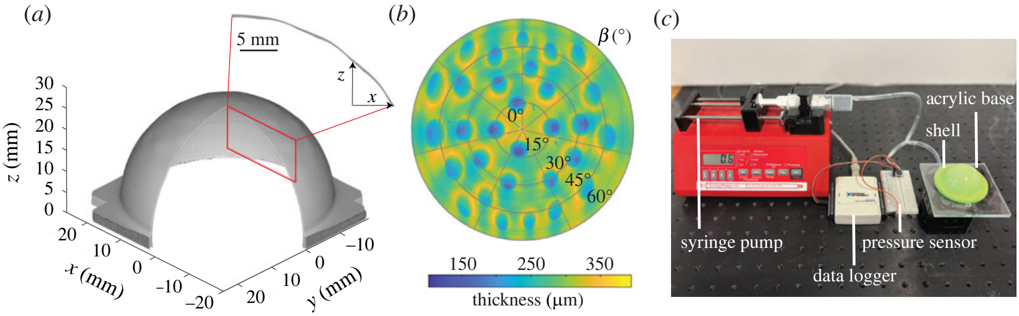

Figure 3. Geometric characterization and apparatus used to perform buckling tests of the shell specimens. (*a*) Reconstructed three-dimensional image of a shell obtained using X-ray micro-computed tomography (μCT). Shell 5 (see parameters in table 1) is used as a representative example. Inset: magnification of a cross-sectional cut in the *x*–*z* plane. (*b*) Thickness profile, $t(\beta,\ \theta)$, of the shell shown in (*a*) obtained after post-processing of the μCT data. (*c*) Experimental apparatus used to measure the buckling pressure of the hemispherical shell specimens. (Online version in colour.)

a distribution of defects was peeled from the mould and tested under internal pressure, p_0 (figure 2*d*).

Note that the bumps protruding from the spherical mould act as topographic barriers to the gravity-driven lubrication flow of VPS-32 prior to curing, causing local modifications in both the geometry of the mid-surface and thickness of the otherwise nearly constant film thickness on a spherical substrate. These specifics of the lubrication flow during fabrication are the reason why, in the experiments, we decided to consider imperfections as *outward* bumps instead of the *inward* dimples mentioned in §2. Had we used dimpled (instead of bumpy) moulds, each of the topographic depressions would have acted as a fluid-accumulating basin causing significant increases of the film thickness there. In that case, the shape of the resulting individual defects would be undesirably shaped very differently than the target dimpled profile of equation (2.1). These fabrication limitations underlie our choice for experimental designs with bumpy defects, which are primarily geometric, albeit still with some degree of thickness variation.

(b) Characterization of the geometry of the experimental specimens

For the detailed validation of FEM against experiments, we will require knowledge of the full geometry of the imperfect shell specimens listed in table 1, which we characterized using X-ray μCT. Our equipment (μCT100, Scanco Medical) offers a scanning resolution of 25.4 µm (voxel size). Each specimen is positioned on a 360° rotary stage of the μCT, which, after image processing of a two-dimensional stack of images, yields a volumetric (three-dimensional) reconstruction of the shell using ImageJ [53]. A representative reconstruction of such a three-dimensional image is presented in figure 3*a*, for Shell 5 (cf. table 1). In the inset of figure 3*a*, we present an arbitrary cross-sectional cut of the reconstruction in the *x*–*z* plane, exhibiting the thickness profile of the imperfect shell.

An in-house Matlab [54] algorithm was then employed to post-process the three-dimensional images and obtain several geometric quantities. Specifically, we perform edge detection on the μCT images to extract the inner and outer surfaces of the shell in spherical coordinates $(r,\ \beta,\ \theta)$. These surfaces are represented, respectively, by their inner, $r_{\rm in}(\beta,\ \theta)$, and outer, $r_{\rm out}(\beta,\ \theta)$, radial positions, from which we then compute the radial position of the shell's mid-surface, $r_{\rm m}(\beta,\ \theta) = [r_{\rm out}(\beta,\theta) + r_{\rm in}(\beta,\theta)]/2$, and the shell-thickness profile $t(\beta,\ \theta) = r_{\rm out}(\beta,\theta) - r_{\rm in}(\beta,\theta)$. The edge-detection algorithm requires a segmentation threshold, which is sensitive for the correct determination of t. We calibrate this threshold value using a digital microscope (VHX, Keyence) to independently measure the shell thickness of a $2 \times 10\,\mathrm{mm}^2$ portion of a sacrificial specimen that is cut to expose the cross section. The segmentation threshold is systematically adjusted until the value of t measured by microscopy on this sacrificial sample matches that obtained by image processing of the μCT images on the same sample.

In figure 3*b*, we show a representative measurement of the thickness profile, $t(\beta, \theta)$, for Shell 5. This thickness profile can then be used to quantify the geometry of the imperfections. Owing to the specifics of the fabrication procedure described in §3a, each defect comprises a combination of a geometric imperfection (of the mid-surface, away from a perfect hemisphere) combined with a small degree of a through-thickness imperfection. Defects produced by small bumps ($s < 1$ mm) in the mould had a nearly axisymmetric thickness about their centre. By contrast, larger defects had asymmetric thicknesses due to VPS-32 polymer accumulating upstream of the bump in the gravity-driven lubrication flow during coating. The full geometric profiles of each of the fabricated shells listed in table 1 were characterized thoroughly using the μCT. Further characterizing individual defects by decoupling the geometric and through-thickness imperfections is beyond the scope of the present work. Instead, the full three-dimensional geometry characterized experimentally was imported into the FEM simulation, allowing for a direct and accurate comparison of the buckling pressures between physical and numerical experiments for validation purposes (see §5).

Eventually, we will report experimental results for the knockdown factor, defined in equation (1.2) as $\kappa = p_{\text{max}}/p_{\text{c}}$, for all of the fabricated specimens. The protocol to measure p_{max} will be detailed below, in §3c. Still, to compute κ, we will also need p_{c}, the classic theoretical prediction for a perfect shell defined in equation (1.1) and, consequently, a nominal value of the thickness, t_0, for the case without defects. For this purpose, we fabricated five nearly perfect (no defects) shells using a stainless steel sphere as the mould ($R = 25.4$ mm, the same as the nominal radius of the three-dimensionally printed moulds). The conditions for the preparation of the VPS-32 solution, pouring and curing were identical to the case of imperfect shells described above. A spherical cap was cut from these nearly perfect shells at $\beta = 45^\circ$ and the thickness was measured using the digital microscope to be $t_0 = 300 \pm 10\ \mu\text{m}$ ($\eta = R/t_0 = 85$).

(c) Measurement of the critical buckling pressure

After fabrication and μCT scanning, we measured the critical buckling pressure of each of the imperfect shell specimens listed in table 1, using an experimental protocol identical to that developed in our previous work [28,33,34,51]. For completeness, we summarize this protocol next.

In figure 3*c*, we show a photograph of the experimental apparatus. A shell specimen was mounted onto an acrylic plate, sealing its equator with a thin layer of VPS-32 polymer. The thick equatorial lip of the shell, together with this layer of VPS-32, enforced clamped boundary conditions at the equator. An additional thin water film was deposited at the joint between the shell equator and the acrylic plate to achieve airtightness. The centre of the acrylic-plate mount contains a through-hole and is connected to a syringe pump (NE-300, New Era Pump Systems, Inc.), a pressure sensor (HSCDRRN005NDAA5, Honeywell Sensing and Productivity Solutions), which is itself linked to a data logger (NI USB-6009, National Instruments). This system is used to depressurize the shell specimen by withdrawing air using the syringe pump (at the constant rate of $0.6\ \text{ml}\ \text{min}^{-1}$), while recording the internal-pressure signal using the pressure sensor and the data logger. The gradual increase of the pressure differential between the inside of the shell and the outside (at atmospheric pressure) eventually causes the shell to buckle at the critical value, p_{max}, past which the measured pressure drops sharply.

Each shell specimen is tested 10 times for quantification of the experimental uncertainties, and the average value is reported. The experimental measurements of p_{max} for each of the specimens listed in table 1 will be reported in §5 (figure 4*b*).

4. Methods: finite-element modelling

In parallel to the experiments, we performed FEM simulations using the commercial package ABAQUS/Standard [55]. In previous works for shells with a single defect [28,30,34,51],

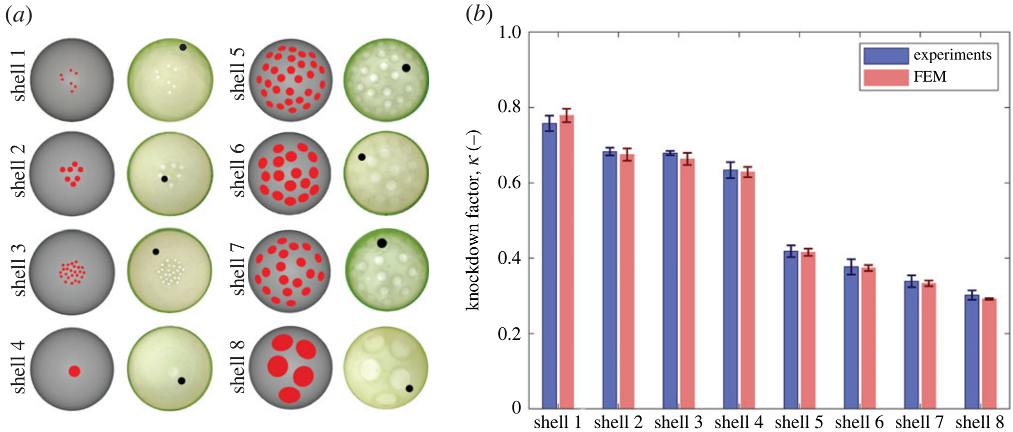

Figure 4. Validation of the FEM simulations against experiments. (*a*) Top views of each of the imperfect shells, showing both the design drawing (left columns) and the corresponding photograph of the fabricated shells (right columns). On the photographs, a black marker indicates the location where buckling occurs immediately past p_{max}. (*b*) Plot of the knockdown factor, κ, for each of the shells tested in the experiments (blue bars) and computed in FEM (red bars). Additional information on the error bars is provided in the text. In both (*a*) and (*b*), the labels—'Shell 1' . . . 'Shell 8'–correspond to table 1. (Online version in colour.)

symmetries were exploited to reduce computational costs. By contrast, the spatial distribution of imperfections in the present study requires the numerics to be tackled as fully three-dimensional. We used S4R shell elements with reduced integration points, allowing for finite membrane strains. The hemispherical shell is divided into four quarters, each composed of 150 elements in both the meridional and azimuthal directions. This discretization choice was deemed appropriate after a mesh-convergence study and will be supported further by the successful validation against experiments (§5). We employed a static Riks solver, selecting an initial arc length of increment of 10^{-1}, with minimum and maximum increment sizes of 10^{-5} and 0.5, respectively. Throughout, geometric nonlinearities were considered. The VPS-32 elastomer was modelled as a neo-Hookean solid with a Poisson's ratio of $\nu = 0.5$ (assuming incompressibility) and a Young's modulus of $E = 1.25 \pm 0.01$ MPa (the measured experimental value).

We recall that the FEM simulations were tackled in two stages. First, we performed a direct validation against experiments (using the experimentally measured geometries); these validation results are provided in §5. Then, having built trust on the simulations upon their successful validation, the FEM was employed for the thorough investigation of the problem defined in §2 using more idealized geometries; these results are provided in §§6 and 7.

For the validation-purposed simulations, the three-dimensional geometric models were imported from the μCT scans of the eight experimental specimens listed in table 1. From these scans, as described in §3b, we extracted the hemispherical profiles of the outer radius, r_{out}, inner radius, r_{in}, and thickness, t; all functions of the voxelated spherical coordinates (β, θ). In ABAQUS, it is difficult to generate a mesh directly from these raw μCT data (point clouds). Alternatively, we first meshed a perfect hemispherical shell, where each node was assigned angular positions and a radius. Nodal displacements were imposed on the original hemispherical mesh such that they matched the interpolated from the μCT values of r_{out} for the same angular coordinates. A nodal thickness equal to the interpolated value from the μCT $t(\beta, \theta)$ profile was then applied at each note. Finally, an offset was imposed using the keyword `*OFFSET` to inform ABAQUS that the specified mesh corresponds to the outer surface of the shell elements.

The FEM simulations of the imperfect shells containing Gaussian dimples were done analogously to the validation simulations described above, but with the idealized geometry. First, we created a perfect hemispherical mesh, whose nodes were then displaced according to the desired design set by the parameters $(\langle\bar{\delta}\rangle, \Delta\bar{\delta}, \lambda, \varphi_{\text{min}})$, with each defect shaped according to equation (2.1). In this case, since the topography of imperfections is specified at the middle surface of the shell, no offset needs to be imposed on the reference surface mesh. In all of these simulations of dimpled shells with $N \geq 2$, a constant nodal thickness is applied to each node, which was fixed such that $\eta = 110$.

5. Validation of the FEM simulations

To gain confidence in the high-fidelity of our three-dimensional FEM simulations, we followed two stages. First, we performed a verification against published results for the one-defect case. Then we validated the FEM simulations against the experiments described in §3.

The first verification stage against existing results is important because the previous studies in [28,30,51], for shells containing only one defect at the pole, made use of circular symmetry (about the vertical axis). Hence, these previous simulations simplified the computational domain to be axisymmetric (two-dimensional) to reduce computational cost. By contrast, the present simulations were designed for the many-defects problem, using three-dimensional shell elements, and involving a fully three-dimensional non-axisymmetric geometry. For the case of one defect located at the pole ($\beta = 0$), we compared the present three-dimensional FEM to the previous two-dimensional FEM results [28], for different values of $\bar{\delta}$ and λ, obtaining, not surprisingly, excellent quantitative agreement between the two. Additional simulations were performed for different polar locations of the defect (while also varying $\bar{\delta}$ and λ), finding that κ remained unmodified as long as the defect was located within $0 \leq \beta \leq 60^\circ$; closer to the equator, interactions with the clamped boundary become important. We recall that in [28], with the defect at the pole, boundary effects were deemed negligible by comparing the FEM results for a hemispherical shell with shell-theory predictions for a complete spherical shell. Shells with the even more restrictive value of $\beta_{\max} = 20^\circ$ will be considered below (cf. table 1), but that choice will also present some issues. Therefore, the value of $\beta_{\max} = 60^\circ$ was kept constant through the subsequent simulations of shells with two defects (§6) and with random distributions of defects (§7).

Having built up trust in the three-dimensional FEM for the one-defect case, we now perform a validation against experiments by comparing the simulated and measured values of the knockdown factor, κ, for each of the eight shells listed in table 1. In figure 4*a*, we present top views of the imperfect shells, showing both the design drawing (left columns, where we highlight the location of the defects), and the corresponding photographs (right columns) of the fabricated shells. In figure 4*b*, we plot the experimentally measured and FEM-computed values of κ (blue and red bars, respectively) for each of the shells. The error bars in the experimental results correspond to the standard deviation of 10 tests, and those for FEM correspond to the propagation of errors originating from the experimental uncertainty in Young's modulus of the VPS-32 elastomer ($E = 1.25 \pm 0.01$ MPa). The typical uncertainties of κ ($\approx 3\%$ for experiments and $\approx 2\%$ for FEM) convey the high precision of our framework. At this stage, the specimens are representative choices, exploring broadly the wide range of possible parameters and no structure should be inferred from the data. Therefore, the identification labels of each shell were simply ordered with decreasing κ. A systematic investigation of parameters will follow in §§6 and 7. What is important to appreciate in figure 4*b* is the remarkable agreement between experiments and FEM, within a few per cent; the discrepancies are at most 3.4% (for Shell 8) and as low as 0.7% (for Shell 5), and more typically ≈ 1–2% for the other shells.

In each of the photographs in figure 4*a*, we have also manually marked (with a black dot) the locus of the buckling event observed immediately past $p_{\max}$. In general, shells containing a distribution of defects with $\lambda < 1$ and delimited by $\beta_{\max} = 20^\circ$ (e.g. Shells 1 and 3) tend to buckle away from the location of the bumpy defects. By contrast, shells with $\lambda > 1$ and delimited by $\beta_{\max} = 60^\circ$ (e.g. Shells 6 and 8) buckle within, or in the proximity of, the designed region of imperfections. The fact that the values of κ are in excellent agreement between experiments and FEM conveys that this qualitative difference is not due to experimental artefacts induced during fabrication. Still, to ensure that the buckling capacity is dictated by the designed regions of imperfections (within $\beta_{\max}$), and not by other subtler effects, we set

$\beta_{\max} = 60^\circ$. Further rationalizing the buckling location goes beyond the scope of the present work.

6. Buckling of imperfect shells containing two defects

Having established our methodology and validated the FEM against experiments, we proceed by focusing on the simulations to study the buckling of shells containing only two defects. We investigate the effect of defect–defect interactions in dictating the knockdown factor, compared with the one-defect case. These results will be important in §7 when interpreting the more complex case of shells containing many imperfections.

First, we consider two identical defects (with the same amplitudes $\overline{\delta} = \overline{\delta}_1 = \overline{\delta}_2$ and normalized widths $\lambda = \lambda_1 = \lambda_2$). The angular distance, φ, between the two defects is varied systematically while setting one at the pole ($\beta_1 = 0$) and the other at $\beta_2 = \varphi$. In figure 5*a*,*b*, we plot the knockdown factor, κ, as a function of φ for the cases of relatively narrow ($\lambda = 1$) and wide ($\lambda = 3$) defects, respectively. Three values of defect amplitude are considered: $\overline{\delta} = \{0.5, 1.0, 1.5\}$ (see legend). As φ increases, κ first decreases to a minimum (the shell weakens) and then increases (the shell strengthens), surpassing the initial value of $\kappa(\varphi = 0)$ to reach a maximum. After this maximum, κ asymptotes to a constant for larger values of φ. This non-monotonic dependence of the buckling strength can be attributed to cross-interactions when the defects are nearby. Important interactions occur for $\varphi \lesssim 20^\circ$ (shaded regions in figure 5*a*,*b*), whereas a plateau with constant κ is observed for $\varphi \gtrsim 20^\circ$. Within the interaction regime, there are both weakening effects (near $\varphi \approx 0$) and strengthening effects (for intermediate angular distances, $12^\circ \lesssim \varphi \lesssim 20^\circ$) with respect to the equivalent one-defect case. Recalling the shape of the individual Gaussian dimple assumed in equation (2.1), the combined profile when $N = 2$ is

$$w(\beta, \theta) = w_1(0, 0) + w_2(\varphi, \theta_2). \tag{6.1}$$

Near $\varphi \approx 0$, the weakening effect can be attributed to the near superposition of the profiles of the two defects, with an amplitude that is nearly twice that of the individual defects. The strengthening effect can be attributed to the potential restrain of the expected buckling mode of one of the defects by the other. Importantly, for $\varphi > 20^\circ$, the plateau of constant κ coincides with that of a shell containing a single defect of the same $\overline{\delta}$ and λ (solid, dashed and dotted horizontal lines in figure 5; see legend), as studied previously in [28]. Thus, when the two defects are sufficiently far apart, their interaction is negligible, and one of them acts as the *weakest link* to govern the buckling capacity of the shell.

We now turn to the case when the two defects are different; the geometry of the $i = 1$ defect is kept constant with $\lambda_1 = 1$ and $\overline{\delta}_1 = 1$, while the $i = 2$ defect has $\overline{\delta}_2 = \{1, 3\}$ and $\lambda_2 = \{1, 3, 5\}$. In figure 5*c*,*d*, we present $\kappa(\varphi)$ curves for shells with $\overline{\delta}_2 = 1$, $\overline{\delta}_2 = 3$ and $\lambda_2 = \{1, 3, 5\}$, respectively. Even if less prominently than for the data in figure 5*a*,*b*, we still find a non-monotonic region of interaction with strengthening and weakening effects, past which a constant plateau is reached for all curves. Coincidentally, the value of $\varphi \approx 20^\circ$ for the angular width separating the interaction region and the plateau, is similar to the identical-defects case. We do not believe that this is a general result. It is important to note that, for the two-defects case with different amplitudes ($\overline{\delta}_1 = 1, \overline{\delta}_2 = 3$) plotted in figure 5*d*, the $\kappa(\varphi)$ curves become nearly flat with increasing width of the $i = 2$ defect ($\lambda_2 = \{3, 5\}$), wider than $\lambda_1 = 1$ for the first defect, even for $\varphi \lesssim 20^\circ$. This result indicates the defects tend to interact more prominently when they have similar geometries.

In both of the $N = 2$ cases explored above (identical and different defects), the exact values of the knockdown factor in the interaction region (strengthening and weakening) and in the plateau depend on the specific geometric properties of the two defects. Developing predictive knowledge for these non-trivial defect–defect interactions deserves a detailed investigation of its own, which is, however, beyond the scope of the present study. Still, the most important feature to retain from the above results is that the values of the plateau are dictated by the strongest defect, highlighting the dominance of the *weakest link* in dictating the buckling of the

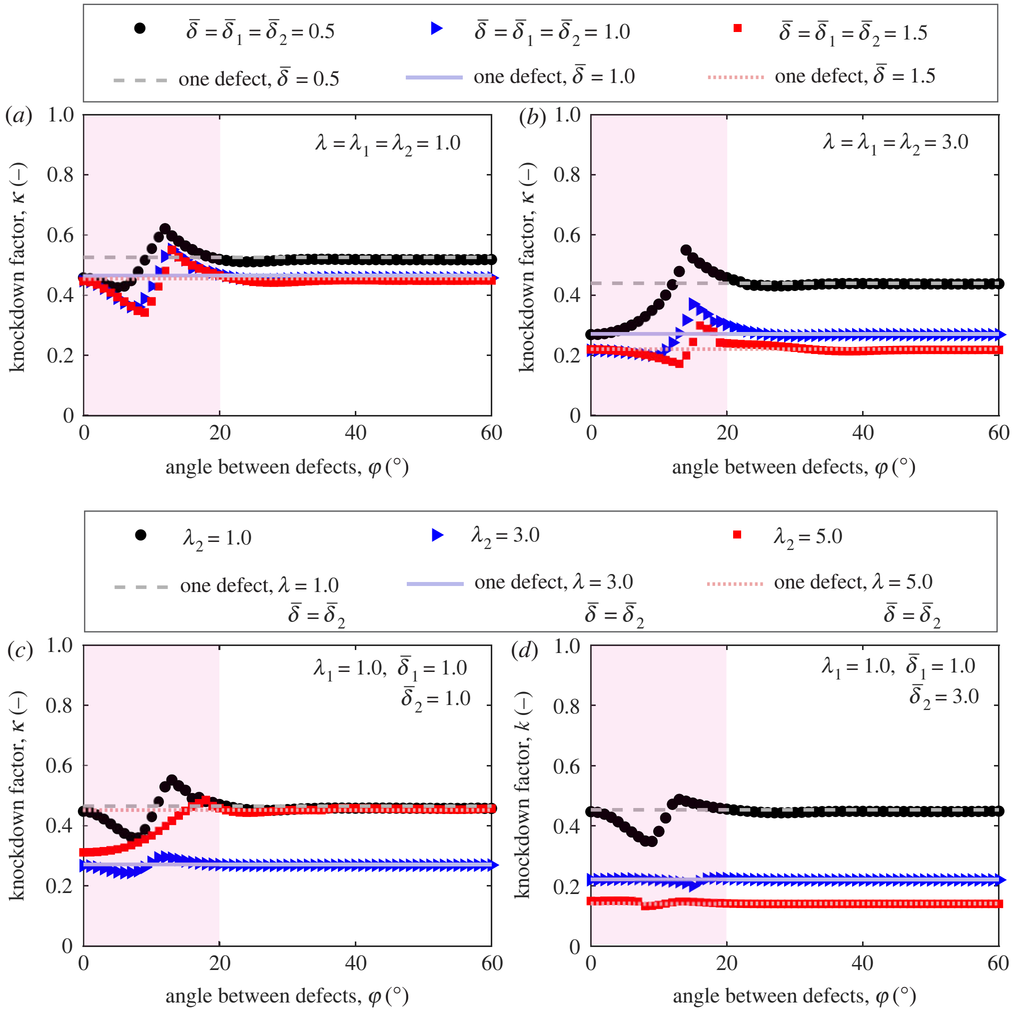

Figure 5. Knockdown factors, κ, versus angular separation between defects, φ, for imperfect shells containing two imperfections ($N = 2$). The shaded areas represent the region where the defects interact. (*a*,*b*) Two *identical* defects with constant normalized width (*a*) $\lambda = \lambda_1 = \lambda_2 = 1$ or (*b*) $\lambda = \lambda_1 = \lambda_2 = 3$, and varying amplitude $\bar{\delta}$ (see legend). (*c*,*d*) Two *distinct* defects with constant $(\bar{\delta}_1,\ \lambda_1) = (1,\ 1)$, but (*c*) $\bar{\delta}_2 = 1$, or (*d*) $\bar{\delta}_2 = 3$, while varying λ_2 at each shell (see legend). The horizontal lines represent the knockdown factors for shells containing a single defect with $(\bar{\delta},\ \lambda) = (\bar{\delta}_2,\ \lambda_2)$. (Online version in colour.)

shells when defects are sufficiently far apart but with more non-trivial interactions when they are nearby.

7. Buckling of imperfect shells containing a distribution of defects

We are now ready to tackle our central problem, defined in §2, of the buckling of shells with a large number of imperfections ($N \gg 1$). These shells contain defects, each of amplitude $\bar{\delta}_i$, which is distributed lognormally according to the PDF, $f(\bar{\delta}_i)$, in equation (2.5), with mean amplitude $\langle\bar{\delta}\rangle$ and standard deviation $\Delta\bar{\delta}$. The explored sets of these parameters are: $\langle\bar{\delta}\rangle = \{0.2, 0.5, 1, 1.5, 2, 2.5, 3\}$ and $\Delta\bar{\delta} = \{0, 0.1, 0.3, 0.6, 1\}$. For each shell design, we fix the defect width $\lambda = \{1, 2\}$ and the minimum angular separation between any two defects $\varphi_{\min} = \{10°, 25°\}$. Recalling that the threshold for defect–defect interactions in the $N = 2$ case is $\varphi_{\min} \approx 20°$ (cf. figure 5), the two values of $\varphi_{\min}$ were chosen to explore configurations where defect–defect interactions are expected to be negligible (for $\varphi_{\min} = 25^\circ$) or important (for $\varphi_{\min} = 10^\circ$). Seeding is done within a spherical cap with $\beta_{\max} = 60^\circ$ to avoid boundary effects. For each set of design parameters ($\langle\bar{\delta}\rangle$, $\Delta\bar{\delta}$, λ, $\varphi_{\min}$), we typically construct 200 realizations of statistically equivalent shell geometries, yielding a total of 28 000 FEM simulations. Only for the data in figure 6, we generated 1200 realizations per shell design to enhance the statistics and check for independence of the ensemble size.

In figure 6*a*1, we show an example of the *input* statistics for a design with ($\langle\bar{\delta}\rangle$, $\Delta\bar{\delta}$, λ, $\varphi_{\min}$) = (1.0, 0.3, 1, 25°). We perform FEM simulations for each of the 1200 statistically equivalent designs, measure the corresponding knockdown factors, κ, and construct the *output* PDF, $f(\kappa)$, shown in figure 6*a*2. We find that the histogram obtained from the FEM data is described well by a 3-parameter Weibull distribution [56] (solid line):

$$f(\kappa) = \frac{\gamma}{\tilde{\kappa}}\left(\frac{\kappa-\kappa_{\min}}{\tilde{\kappa}}\right)^{\gamma-1}\exp\left(-\left(\frac{\kappa-\kappa_{\min}}{\tilde{\kappa}}\right)^{\gamma}\right), \tag{7.1}$$

where $\tilde{\kappa}$, γ and $\kappa_{\min}$ are the scale, shape and location (threshold) parameters, respectively. The third fitting parameter, $\kappa_{\min}$, is required to account for the lower bound of κ, associated with the plateau of the $\kappa(\bar{\delta})$ curves, which was investigated in [29] for single-defect shells and found to depend on λ and η. In figure 6*b*1, a second example with ($\langle\bar{\delta}\rangle$, $\Delta\bar{\delta}$, λ, $\varphi_{\min}$) = (1.0, 0.3, 1, 10°) also yields Weibull statistics for the knockdown factor (figure 6*b*2).

The three Weibull fitting parameters ($\tilde{\kappa}$, γ, $\kappa_{\min}$) used to plot the Weibull distribution in figure 6*a*2 and 6*b*2 were obtained based on the Maximum Likelihood Estimates (`*mle` function in Matlab) and determined to be (0.012, 3.242, 0.433) and (0.119, 5.663, 0.372), respectively. Using these fitting parameters, we also computed the corresponding Weibull cumulative distribution functions (CDFs),

$$F(\kappa) = 1 - \exp\left(-\left(\frac{\kappa-\kappa_{\min}}{\tilde{\kappa}}\right)^{\gamma}\right), \tag{7.2}$$

which are in excellent agreement with the histograms obtained from the FEM data, as shown in figure 6*a*3,*b*3. As a double-check, if the FEM data for the $F(\kappa)$ statistics are indeed represented by a Weibull CDF, plotting $\ln(\ln(1/(1-F(\kappa))))$ as a function of $\ln(\kappa-\kappa_{\min})$ is expected to yield a straight line of slope γ, which is confirmed in figure 6*a*4,*b*4 for the $\varphi_{\min} = 25^\circ$ and $\varphi_{\min} = 10^\circ$ cases, respectively.

The Weibull distribution functions in equations (7.1) and (7.2) are derived based on extreme value theory [57], under the assumption that the failure probability of one representative element of a structure follows a power-law tail [58]. Within this framework, the failure of one of the elements, the *weakest link*, yields the global failure of the structure [58–62]. The above observations from the data in figure 6 indicate the suitability of the 3-parameter Weibull distribution to describe the statistics of the knockdown factors of shells with lognormally distributed defect amplitudes, suggesting that probabilistic shell buckling can be placed within the class of extreme-value phenomena.

In figure 7, we now plot a set of PDFs, $f(\kappa)$, obtained by fitting the FEM data similarly to what was done in figure 6, for a wider range of the parameters $\langle\bar{\delta}\rangle$ and $\Delta\bar{\delta}$. For clarity, we only show the fitted PDFs and not the actual histograms of the FEM data. The data in figure 7*a*,*b* explore various $\Delta\bar{\delta}$, $0.0 \le \Delta\bar{\delta} \le 1.0$ (while fixing $\langle\bar{\delta}\rangle = 1.0$). In figure 7*c*,*d*, we explore various $\langle\bar{\delta}\rangle$, $0.2 \le \langle\bar{\delta}\rangle \le 3.0$ (while fixing $\Delta\bar{\delta} = 0.3$). Panels (*a*, *c*) are for $\varphi_{\min} = 25^\circ$ and panels (*b*, *d*) are for $\varphi_{\min} = 10^\circ$. First, the data in figure 7*a*, with fixed $\langle\bar{\delta}\rangle = 1.0$, show that the mode (location of the peak) of $f(\kappa)$ remains approximately constant, for all $\Delta\bar{\delta}$, even if the peak probability decreases slightly with $\Delta\bar{\delta}$. In figure 7*b*, when the minimum defect-to-defect distance is decreased to $\varphi_{\min} = 10^\circ$, we find that κ decreases with $\Delta\bar{\delta}$, presumably due to the higher probability of randomly seeding defect amplitudes from the high tail of $f(\bar{\delta}_i)$, coupled with defect–defect interactions. Furthermore, the fitted Weibull threshold decreases consistently with increasing $\Delta\bar{\delta}$. Similarly, when fixing $\Delta\bar{\delta} = 0.3$ and increasing the defect amplitude $\langle\bar{\delta}\rangle$ (figure 7*c*,*d*), we find a modest decrease in κ for $\varphi_{\min} = 25^\circ$ (figure 7*c*), where the strongest defect governs most of the shell behaviour. For $\varphi_{\min} = 10^\circ$ (figure 7*d*), this behaviour is more pronounced due to defect–defect interactions.

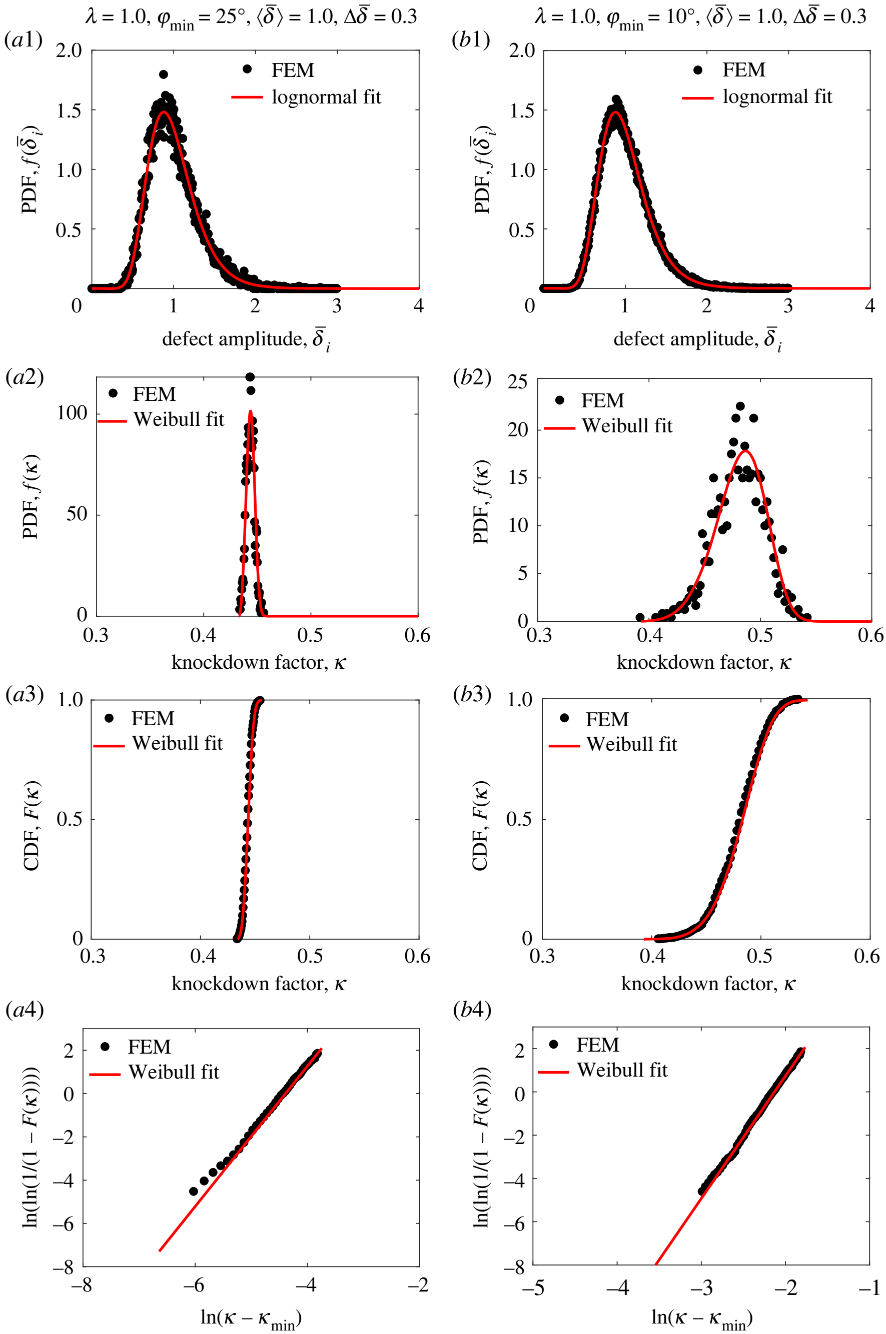

Figure 6. Probabilistic buckling of a shell containing a distribution of defects. (*a*1, *b*1) Input probability density functions (PDFs) of the amplitude of defects, $f(\bar{\delta}_i)$, used for the shell design. (*a*2, *b*2) Output PDFs of knockdown factor, $f(\kappa)$. (*a*3, *b*3) Cumulative distribution functions (CDFs) of κ, $F(\kappa)$. (*a*4, *b*4) Weibull plots of $F(\kappa)$. The minimum angular separation between any two defects is set to $\varphi_{\min} = 25^\circ$ in panels (*a*1–*a*4) and to $\varphi_{\min} = 10^\circ$ in panels (b1-b4). All other design parameters are kept fixed at $\lambda = 1$, $\bar{\delta} = 1.0$ and $\Delta\bar{\delta} = 0.3$. The PDFs in panels (*a*1, *b*1) were constructed using 500 bins. The PDFS in panels (*a*2–*a*4) were constructed with 2000 bins, and those in (*b*2–*b*4) with 500 bins, due to their different span across the considered range $0.3 \leq \kappa \leq 0.6$. (Online version in colour.)

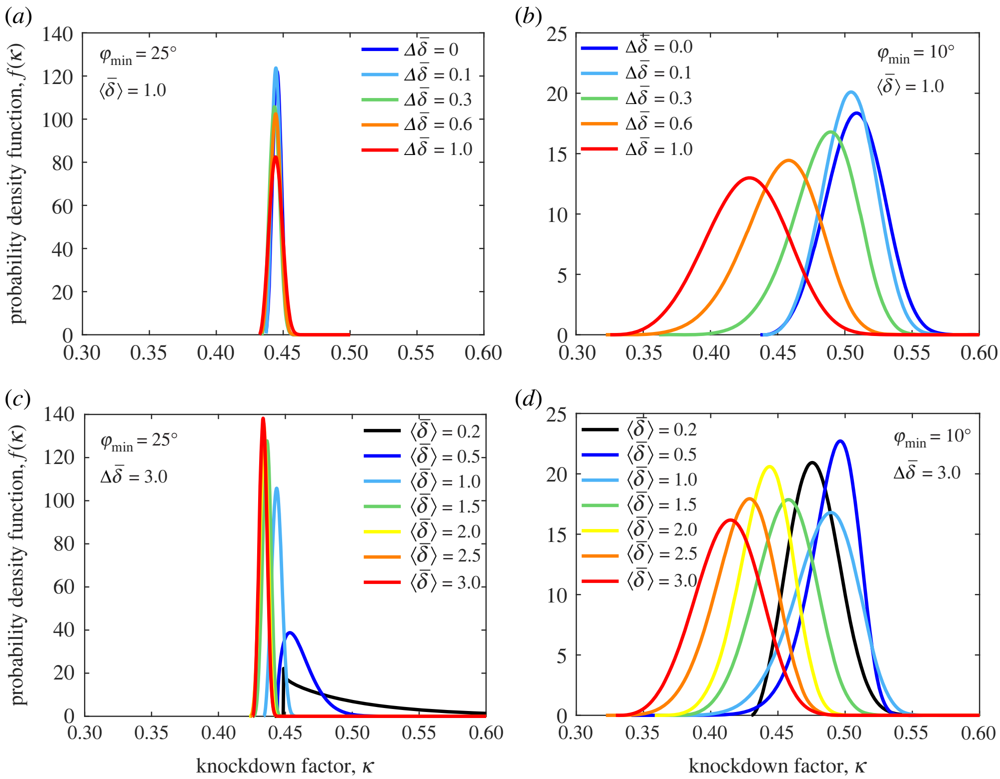

Figure 7. Probability density functions of the knockdown factor, $f(\kappa)$, obtained by fitting equation (7.1) to the FEM data, for a variety of design parameters. (*a*,*b*) Constant amplitude $\langle\bar{\delta}\rangle = 1$ and varying $0 \le \Delta\bar{\delta} \le 1.0$ (see legend); for (*a*) $\varphi_{min} = 25°$ and (*b*) $\varphi_{min} = 10°$. (*c*,*d*) Constant value of $\Delta\bar{\delta} = 0.3$ and varying $0.2 \le \langle\bar{\delta}\rangle \le 3.0$; for (*c*) $\varphi_{min} = 25°$ and for (*d*) $\varphi_{min} = 10°$. (Online version in colour.)

It is of interest to quantify the mode, κ^*; i.e. location of the peak of $f(\kappa)$, for all of our data. In figure 8, we plot κ^* as a function of the mean defect amplitude, $\langle\bar{\delta}\rangle$, for four different design configurations. Figure 8*a*,*b* corresponds to $\varphi_{min} = 25°$, and panels (*c*,*d*) to $\varphi_{min} = 10°$. Also, panels (*a*,*c*) are for $\lambda = 1.0$, and panels (*b*,*d*) for wider defects with $\lambda = 2.0$. The various datasets (see legend) have different values of $\Delta\bar{\delta}$. In all plots, the dotted lines represent results for a shell with a single defect of amplitude $\langle\bar{\delta}\rangle$. These FEM data for one-defect shells were verified with the data in [28].

Focusing first on figure 8*a*, we find that the mode of the knockdown factor, κ^*, decreases with increasing $\Delta\bar{\delta}$, due to the higher probability of seeding deeper, and hence more dominant, defects in the high tail of $f(\bar{\delta}_i)$ for higher values of $\Delta\bar{\delta}$. This decrease of κ^* is more pronounced when $\langle\bar{\delta}\rangle \lesssim 1$ and less so in the plateau region, for $\langle\bar{\delta}\rangle > 1$. The plateau has an approximate constant value $\kappa^* \approx 0.45$, which is in agreement with predictions of the analogous plateau for single-defect shells [29]. These findings suggest that the buckling capacity of shells containing a distribution of imperfections is dominated by the deepest defect, their *weakest link*. This scenario is qualitatively similar when $\lambda = 2$, as shown in figure 8*b*, where the plateau region also matches the single-defect case. These various features are slightly different for the datasets in figure 8*c*,*d*, when $\varphi = 10°$. Here, for example, the dataset with $\Delta\bar{\delta} = 0$ (circles) does not coincide with the one-defect curve (dotted line), especially for $\lambda = 2$ (figure 8*d*), which can be attributed to defect–defect interactions. Moreover, when $\varphi = 10°$, the resultant plateau of κ^* is consistently below that of shells with a single defect [29], especially in figure 8*d*, further indicating the importance of defect–defect interactions in this regime.

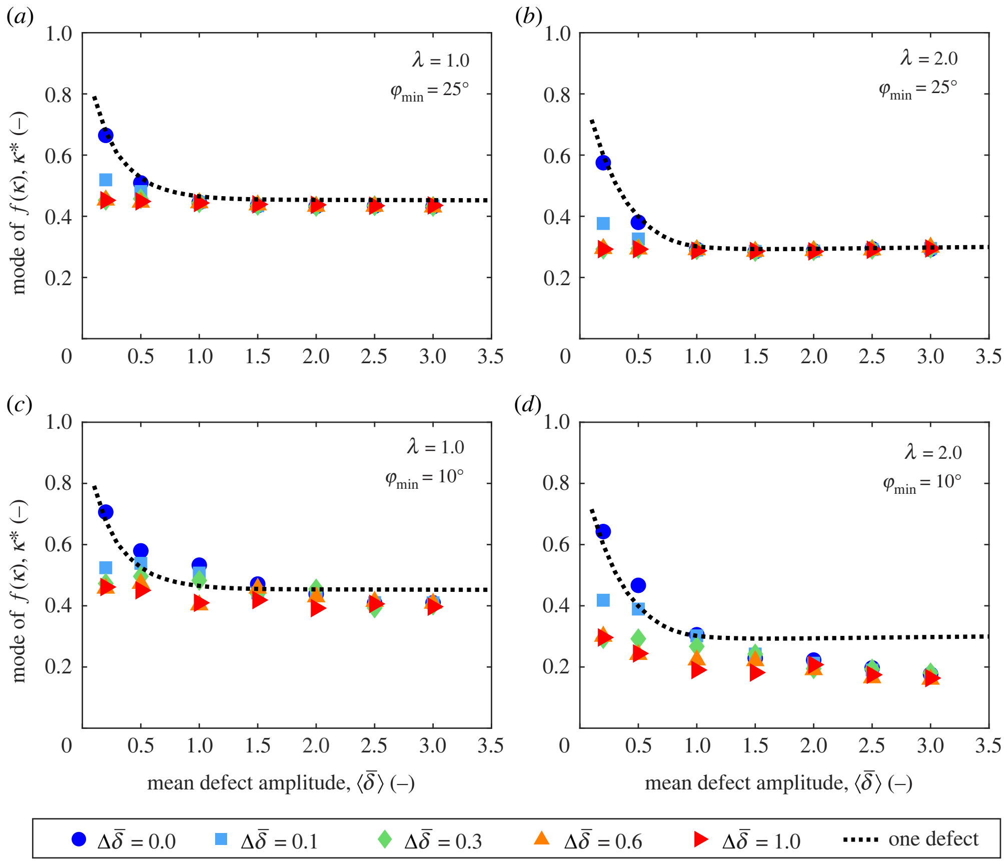

Figure 8. Mode of knockdown factors, κ^*, versus the mean defect amplitude, $\langle\bar{\delta}\rangle$. (*a,b*) $\varphi_{\min} = 25^\circ$ (non-interacting defects) and widths $\lambda = 1$ and $\lambda = 2$, respectively. (*c,d*) $\varphi = 10^\circ$ (interacting defects) and widths $\lambda = 1$ and $\lambda = 2$, respectively. The various datasets correspond to different values of $\Delta\bar{\delta}$ (see legend), and are compared with the equivalent single-defect cases (dotted lines). (Online version in colour.)

Returning to the PDFs presented in figure 7, we observe qualitatively that the $f(\kappa)$ distributions are typically narrow for $\varphi = 25^\circ$ (when there are *negligible* defect–defect interactions; e.g., figure 7*a*) and broad for $\varphi = 10^\circ$ (when there are *significant* defect–defect interactions; e.g. figure 7*b*). In the final step of our investigation, we seek to quantify the width of the $f(\kappa)$ distributions, as measured by the standard deviation of the resultant knockdown factor, $\Delta\kappa$, for a variety of design parameters. The corresponding data are shown in figure 9. With *negligible* defect–defect interactions ($\varphi = 25^\circ$; see figure 9*a,b*), $f(\kappa)$ remains consistently narrow ($\Delta\kappa$ is small) when $\langle\bar{\delta}\rangle \gtrsim 1$, but broadening occurs for $\langle\bar{\delta}\rangle \lesssim 1$, significantly more so for the larger values of $\Delta\bar{\delta}$. This behaviour is robust for the two values of λ explored in figure 9*a,b*. By contrast, when there are *important* defect–defect interactions ($\varphi = 10^\circ$; see figure 9*c,d*), $f(\kappa)$ is always broad across most of the range of $\langle\bar{\delta}\rangle$, and fairly independent of $\Delta\bar{\delta}$. From the perspective of structural reliability, these results highlight the following possible interpretation scenario. Shells with non-interacting defects with large amplitudes ($\langle\bar{\delta}\rangle \gtrsim 1$) appear to exhibit quasi-deterministic buckling, with narrow $f(\kappa)$ distributions. By contrast, shells with either small-amplitude defects ($\langle\bar{\delta}\rangle \lesssim 1$) or interacting defects exhibit a far more probabilistic behaviour, with broad $f(\kappa)$ distributions, and have, therefore, significantly lower reliability.

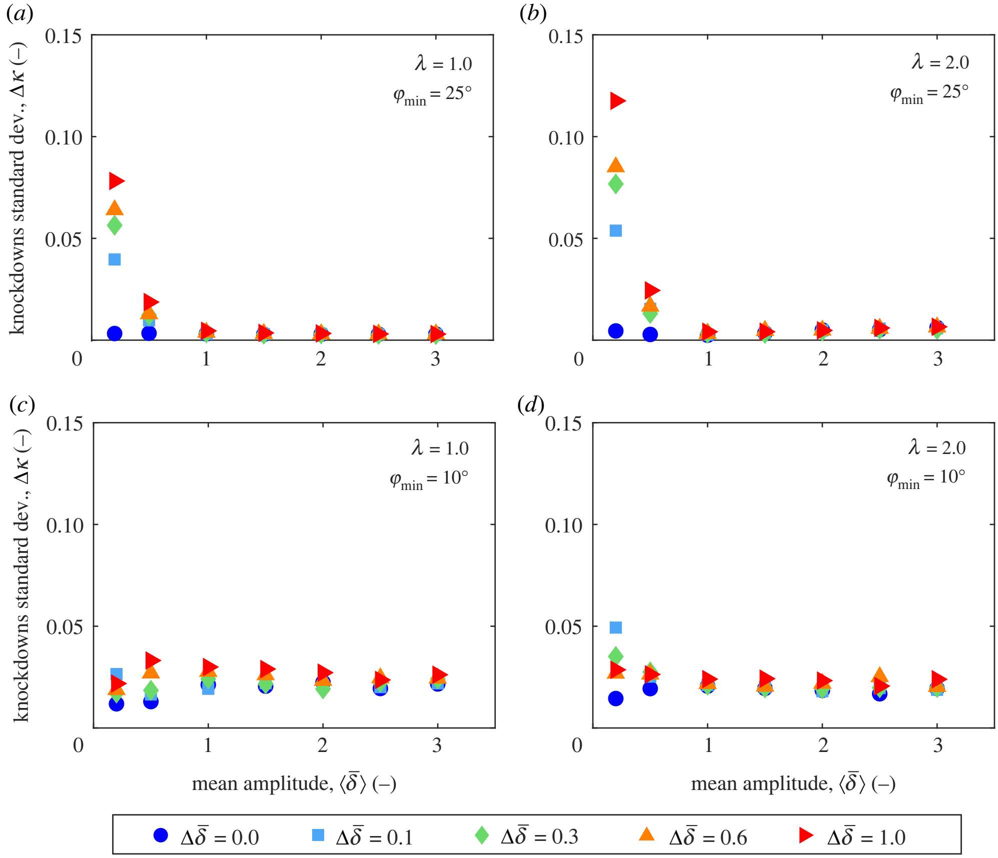

Figure 9. Standard deviation of the resultant knockdown factors, $\Delta\kappa$, versus the mean defect amplitude, $\langle\bar{\delta}\rangle$. (*a*,*b*) $\varphi_{\mathrm{min}} = 25^\circ$ (non-interacting defects) and widths $\lambda = 1$ and $\lambda = 2$, respectively. (*c*, *d*) $\varphi = 10^\circ$ (interacting defects) and widths $\lambda = 1$ and $\lambda = 2$, respectively. The various datasets correspond to different values of $\Delta\bar{\delta}$ (see legend). (Online version in colour.)

8. Discussions and Conclusion

We have employed experimentally validated FEM simulations to investigate the buckling of spherical shells containing a random distribution of defects, seeking to quantify the resultant knockdown factor (κ) statistics, as measured by the probability density function, $f(\kappa)$. First, we used three-dimensionally printed moulds and a polymer coating technique to fabricate imperfect hemispherical shells containing distributions of defects. The imperfections comprised *outward* defects (bumps) and the full geometry of the shell was characterized through μCT. Using the μCT geometric data, a high-fidelity three-dimensional shell FEM was validated against experimental buckling measurements.

After validating the FEM, we first focused on imperfect shells containing only two defects ($N = 2$) to characterize the influence of defect–defect interactions on the buckling conditions. The results showed these interactions can be significant when the angular separation between the two defects is below a threshold value ($\varphi \lesssim 20^\circ$). Within this regime of interactions, we observed both weakening (near $\varphi \approx 0$) and strengthening (for intermediate angular distances, $12^\circ \lesssim \varphi \lesssim 20^\circ$) effects. When the defects are further apart, outside of the interactions regime ($\varphi \gtrsim 20^\circ$), the knockdown factor tends to a constant value, coinciding with the equivalent one-defect case. In the absence of defect–defect interactions, this result indicates that the shell buckling is dictated by the strongest defect of the pair—its *weakest link*.

We then focused on the central part of our study, where multiple defects ($N \gg 1$) were distributed randomly on the surface of the spherical shell. The amplitude $\bar{\delta}_i$ of each defect was treated as a random variable sampled from a lognormal distribution of mean $\langle\bar{\delta}\rangle$, and standard deviation $\Delta\bar{\delta}$, while fixing the defect width and the minimum defect–defect angular separation for each shell design. In what we see as the most important contribution of this work, we find that, given a set of design parameters of shells containing many defects (whose amplitudes are lognormally distributed), the statistics of the resultant knockdown factor are described by the 3-parameter Weibull distribution, $f(\kappa)$ in equation (7.1). This result is consistent with other extreme-value statistics problems where, in their general form, an *input* distribution of *links*, whose individual failure probability follows a power-law tail, yields an *output* Weibull distribution [58,63]. Further analysing the resultant Weibull distribution, for all input $\langle\bar{\delta}\rangle$ and $\Delta\bar{\delta}$, we found that the output distributions are consistently narrow when there are less prominent interactions between defects ($\varphi_{\min} = 25^\circ$), in comparison with the broader distributions when defect–defect interactions are present ($\varphi_{\min} = 10^\circ$). These findings for the width of $f(\kappa)$, together with the results for its mode, are consistent with the *weakest-link* interpretation where the deepest defect governs the global shell buckling.

In future work, using the approach reported here, we intend to revisit and rationalize the results from the seminal experiments by Carlson *et al.* [18], where increasing knockdown factors were observed when progressively eliminating severe defects. More broadly, we believe that our findings will open an exciting avenue for future study on probabilistic shell buckling, including theoretical methods based on extreme-value statistics and weakest-link models.

Data accessibility. All data generated and analysed during this study are included in this published article.

The data are provided in the electronic supplementary material [64].

Authors' contributions. F.D.: conceptualization, data curation, formal analysis, investigation, methodology, software, validation, visualization, writing—original draft, writing—review and editing; W.G.: data curation, formal analysis, investigation, methodology, software, validation, visualization, writing—review and editing; D.Y.: conceptualization, formal analysis, methodology, software, validation, writing—review and editing; P.M.R.: conceptualization, formal analysis, funding acquisition, investigation, methodology, project administration, resources, supervision, visualization, writing—original draft, writing—review and editing.

All authors gave final approval for publication and agreed to be held accountable for the work performed therein.

Conflict of interest declaration. We declare we have no competing interests.

Funding. No funding has been received for this article.

Acknowledgements. The authors are grateful to Roberto Ballarini and Jia-Liang Le for discussions on extreme-value statistics and their potential connection to shell buckling, which motivated the present study. We also thank Arefeh Abbasi and Luna Lin for a critical read of the present manuscript and for their valuable feedback.

References

1. Lidmar J, Mirny L, Nelson DR. 2003 Virus shapes and buckling transitions in spherical shells. *Phys. Rev. E* **68**, 051910. (doi:10.1103/PhysRevE.68.051910)
2. Katifori E, Alben S, Cerda E, Nelson DR, Dumais J. 2010 Foldable structures and the natural design of pollen grains. *Proc. Natl Acad. Sci. USA* **107**, 7635–7639. (doi:10.1073/pnas.0911223107)
3. Yin J, Cao Z, Li C, Sheinman I, Chen X. 2008 Stress-driven buckling patterns in spheroidal core/shell structures. *Proc. Natl Acad. Sci. USA* **105**, 19 132–19 135. (doi:10.1073/pnas.0810443105)
4. Datta SS, Kim SH, Paulose J, Abbaspourrad A, Nelson DR, Weitz DA. 2012 Delayed buckling and guided folding of inhomogeneous capsules. *Phys. Rev. Lett.* **109**, 134302. (doi:10.1103/PhysRevLett.109.134302)
5. Godoy LA. 2016 Buckling of vertical oil storage steel tanks: Review of static buckling studies. *Thin-Walled Struct.* **103**, 1–21. (doi:10.1016/j.tws.2016.01.026)
6. Hoff N. 1967 Thin shells in aerospace structures: 4th Von Karman lecture. *Astronautics & Aeronautics* **2**, pp. 26–45.

7. Pearson C, Delatte N. 2006 Collapse of the quebec bridge, 1907. *J. Perform. Constr. Facil.* **20**, 84–91. (doi:10.1061/(ASCE)0887-3828(2006)20:1(84))
8. Djellouli A, Marmottant P, Djeridi H, Quilliet C, Coupier G. 2017 Buckling instability causes inertial thrust for spherical swimmers at all scales. *Phys. Rev. Lett.* **119**, 224501. (doi:10.1103/PhysRevLett.119.224501)
9. Gorissen B, Melancon D, Vasios N, Torbati M, Bertoldi K. 2020 Inflatable soft jumper inspired by shell snapping. *Sci. Rob.* **5**, eabb1967. (doi:10.1126/scirobotics.abb1967)
10. Sacanna S, Irvine WTM, Rossi L, Pine DJ. 2011 Lock and key colloids through polymerization-induced buckling of monodisperse silicon oil droplets. *Soft Matter* **7**, 1631–1634. (doi:10.1039/C0SM01125H)
11. Reis PM. 2015 A perspective on the revival of structural (in)stability with novel opportunities for function: from buckliphobia to buckliphilia. *J. Appl. Mech.* **82**, 111001. (doi:10.1115/1.4031456)
12. Zoelly R. 1915 *Ueber ein Knickungsproblem an der Kugelschale*. Doctoral Thesis ETH Zurich. (doi:10.3929/ethz-a-000091951).
13. Tsien HS. 1942 A theory for the buckling of thin shells. *J. Aeronaut. Sci.* **9**, 373–384. (doi:10.2514/8.10911)
14. Kaplan A, Fung YC. 1954 A nonlinear theory of bending and buckling of thin elastic shallow spherical shells. Technical Note 3212 National Advisory Committee for Aeronautics Washington, DC.
15. Homewood R, Brine A, Johnson AE. 1961 Experimental investigation of the buckling instability of monocoque shells. *Exp. Mech.* **1**, 88–96. (doi:10.1007/BF02324071)
16. Seaman L. 1962 *The nature of buckling in thin spherical shells*. Technical report WATERTOWN ARSENAL LABS MA.
17. Krenzke MA, Kiernan TJ. 1963 Elastic stability of near-perfect shallow spherical shells. *AIAA J.* **1**, 2855–2857. (doi:10.2514/3.2187)
18. Carlson R, Sendelbeck R, Hoff N. 1967 Experimental studies of the buckling of complete spherical shells. *Exp. Mech.* **7**, 281–288. (doi:10.1007/BF02327133)
19. Koiter WT. 1945 *Over de stabiliteit van het elastisch evenwicht*. PhD thesis Delft University of Technology Delft, The Netherlands.
20. Hutchinson JW, Muggeridge DB, Tennyson RC. 1971 Effect of a local axisymmetric imperfection on the buckling behavior of a circular cylindrical shell under axial compression. *AIAA J.* **9**, 48–52. (doi:10.2514/3.6123)
21. Budiansky B, Hutchinson JW. 1972 Buckling of circular cylindrical shells under axial compression. In *Contributions to the Theory of Aircraft Structures*, pp. 239–259. The Netherlands: Nijgh-Wolters-Noordhoff University Publishers.
22. Bijlaard PP, Gallagher RH. 1960 Elastic instability of a cylindrical shell under arbitrary circumferential variation of axial stress. *J. Aerosp. Sci.* **27**, 854–858. (doi:10.2514/8.8776)
23. Kobayashi S. 1968 The influence of the boundary conditions on the buckling load of cylindrical shells under axial compression. *J. Jpn Soc. Aeronaut. Eng.* **16**, 74–82. (doi:10.2322/jjsass1953.16.74)
24. Hutchinson JW. 2016 Buckling of spherical shells revisited. *Proc. R. Soc. A: Math., Phys. Eng. Sci.* **472**, 20160577. (doi:10.1098/rspa.2016.0577)
25. Seide P, Weingarten V, Morgan E. 1960 *The development of design criteria for elastic stability of thin shell structures*. Technical report TRW Space Technology Labs Los Angeles CA.
26. Weingarten V, Seide P, Peterson J. 1968 Buckling of thin-walled circular cylinders-NASA SP-8007. *Nasa Spec. Publ.* **8007**. Washington DC.
27. Lee A, Brun PT, Marthelot J, Balestra G, Gallaire F, Reis PM. 2016 Fabrication of slender elastic shells by the coating of curved surfaces. *Nat. Commun.* **7**, 11155. (doi:10.1038/ncomms11155)
28. Lee A, López Jiménez F, Marthelot J, Hutchinson JW, Reis PM. 2016 The geometric role of precisely engineered imperfections on the critical buckling load of spherical elastic shells. *J. Appl. Mech.* **83**, 111005. (doi:10.1115/1.4034431)
29. Jiménez FL, Marthelot J, Lee A, Hutchinson JW, Reis PM. 2017 Technical brief: knockdown factor for the buckling of spherical shells containing large-amplitude geometric defects. *J. Appl. Mech.* **84**, 034501. (doi:10.1115/1.4035665)
30. Yan D, Pezzulla M, Reis PM. 2020 Buckling of pressurized spherical shells containing a through-thickness defect. *J. Mech. Phys. Solids* **138**, 103923. (doi:10.1016/j.jmps.2020.103923)

31. Thompson JMT, Hutchinson JW, Sieber J. 2017 Probing shells against buckling: a nondestructive technique for laboratory testing. *Int. J. Bifurcation Chaos* **27**, 1730048. (doi:10.1142/S0218127417300488)
32. Virot E, Kreilos T, Schneider TM, Rubinstein SM. 2017 Stability landscape of shell buckling. *Phys. Rev. Lett.* **119**, 224101. (doi:10.1103/PhysRevLett.119.224101)
33. Marthelot J, López Jiménez F, Lee A, Hutchinson JW, Reis PM. 2017 Buckling of a pressurized hemispherical shell subjected to a probing force. *J. Appl. Mech.* **84**, 121005. (doi:10.1115/1.4038063)
34. Abbasi A, Yan D, Reis PM. 2021 Probing the buckling of pressurized spherical shells. *J. Mech. Phys. Solids* **155**, 104545. (doi:10.1016/j.jmps.2021.104545)
35. Fan H. 2019 Critical buckling load prediction of axially compressed cylindrical shell based on non-destructive probing method. *Thin-Walled Struct.* **139**, 91–104. (doi:10.1016/j.tws.2019.02.034)
36. Yadav KK, Cuccia NL, Virot E, Rubinstein SM, Gerasimidis S. 2021 A nondestructive technique for the evaluation of thin cylindrical shells' axial buckling capacity. *J. Appl. Mech.* **88**, 051003. (doi:10.1115/1.4049806)
37. Wullschleger L. 2006 *Numerical investigation of the buckling behaviour of axially compressed circular cylinders having parametric initial dimple imperfections*. PhD thesis ETH Zurich.
38. Amazigo JC. 1969 Buckling under axial compression of long cylindrical shells with random axisymmetric imperfections. *Q. Appl. Math.* **26**, 537–566. (doi:10.1090/qam/99838)
39. Elishakoff I, Arbocz J. 1982 Reliability of axially compressed cylindrical shells with random axisymmetric imperfections. *Int. J. Solids Struct.* **18**, 563–585. (doi:10.1016/0020-7683(82)90040-3)
40. Elishakoff I, Arbocz J. 1985 Reliability of axially compressed cylindrical shells with general nonsymmetric imperfections. *J. Appl. Mech.* **52**, 122–8. (doi:10.1115/1.3168980)
41. Elishakoff I. 2012 Probabilistic resolution of the twentieth century conundrum in elastic stability. *Thin-Walled Struct.* **59**, 35–57. (doi:10.1016/j.tws.2012.04.002)
42. Kaplan A, Fung YC. 1954 *A nonlinear theory of bending and buckling of thin elastic shallow spherical shells*. Technical report NACA Technical Note 3212.
43. Koga T, Hoff NJ. 1969 The axisymmetric buckling of initially imperfect complete spherical shells. *Int. J. Solids Struct.* **5**, 679–697. (doi:10.1016/0020-7683(69)90088-2)
44. Surendran S, Tanyimboh TT, Tabesh M. 2005 Peaking demand factor-based reliability analysis of water distribution systems. *Adv. Eng. Softw.* **36**, 789–796. (doi:10.1016/j.advengsoft.2005.03.023)
45. Low YM. 2013 A new distribution for fitting four moments and its applications to reliability analysis. *Struct. Saf.* **42**, 12–25. (doi:10.1016/j.strusafe.2013.01.007)
46. Le JL, Bažant ZP, Bazant MZ. 2011 Unified nano-mechanics based probabilistic theory of quasibrittle and brittle structures: I. Strength, static crack growth, lifetime and scaling. *J. Mech. Phys. Solids* **59**, 1291–1321. (doi:10.1016/j.jmps.2011.03.002)
47. Le JL, Bažant ZP. 2020 Failure probability of concrete specimens of uncertain mean strength in large database. *J. Eng. Mech.* **146**, 04020039.
48. Lopez-Pamies O, Goudarzi T, Danas K. 2013 The nonlinear elastic response of suspensions of rigid inclusions in rubber: II - A simple explicit approximation for finite-concentration suspensions. *J. Mech. Phys. Solids* **61**, 19–37. (doi:10.1016/j.jmps.2012.08.013)
49. Shrimali B, Lefèvre V, Lopez-Pamies O. 2019 A simple explicit homogenization solution for the macroscopic elastic response of isotropic porous elastomers. *J. Mech. Phys. Solids* **122**, 364–380. (doi:10.1016/j.jmps.2018.09.026)
50. Lefèvre V, Lopez-Pamies O. 2017 Nonlinear electroelastic deformations of dielectric elastomer composites: II - Non-Gaussian elastic dielectrics. *J. Mech. Phys. Solids* **99**, 438–470. (doi:10.1016/j.jmps.2016.07.005)
51. Yan D, Pezzulla M, Cruveiller L, Abbasi A, Reis PM. 2021 Magneto-active elastic shells with tunable buckling strength. *Nat. Commun.* **12**, 1–9. (doi:10.1038/s41467-021-22776-y)
52. Weisstein EW. Sphere–sphere intersection. From *MathWorld–A Wolfram Web Resource*. https://mathworld.wolfram.com/Sphere-SphereIntersection.html.
53. Schindelin J *et al.* 2012 Fiji: an open-source platform for biological-image analysis. *Nat. Methods* **9**, 676–682. (doi:10.1038/nmeth.2019)
54. MATLAB. 2021 *version 7.21.0 (R2021a)*. Natick, Massachusetts: The MathWorks Inc.

55. ABAQUS. 2014 Abaqus theory guide. In *Version 6.14*. USA: Dassault Systems Simulia Corp.
56. Weibull W. 2021 A statistical distribution function of wide applicability. *J. Appl. Mech.* **18**, 293–297. (doi:10.1115/1.4010337)
57. Fisher RA, Tippett LHC. 1928 Limiting forms of the frequency distribution of the largest or smallest member of a sample. In *Mathematical proceedings of the Cambridge philosophical society* (ed. BJ Green), vol. 24, pp. 180–190.
58. Le JL, Ballarini R, Zhu Z. 2015 Modeling of probabilistic failure of polycrystalline silicon MEMS structures. *J. Am. Ceram. Soc.* **98**, 1685–1697. (doi:10.1111/jace.13639)
59. Weibull W. 1939 The phenomenon of rupture in solids. *IVA Handlingar* **153, 1–55**.
60. Weibull W. 1951 A statistical distribution function of wide applicability. *J. Appl. Mech.* **18**, 293–297. (doi:10.1115/1.4010337)
61. Bažant ZP, Le JL, Bazant MZ. 2009 Scaling of strength and lifetime probability distributions of quasibrittle structures based on atomistic fracture mechanics. *Proc. Natl Acad. Sci. USA* **106**, 11 484–11 489.
62. Le JL, Bažant ZP. 2009 Strength distribution of dental restorative ceramics: finite weakest link model with zero threshold. *Dent. Mater.* **25**, 641–648. (doi:10.1016/j.dental.2008.11.011)
63. Jayatilaka ADS, Trustrum K. 1977 Statistical approach to brittle fracture. *J. Mater. Sci.* **12**, 1426–1430. (doi:10.1007/BF00540858)
64. Derveni F, Gueissaz W, Yan D, Reis PM. 2023 Probabilistic buckling of imperfect hemispherical shells containing a distribution of defects. Figshare. (doi:10.6084/m9.figshare.c.6373233)